

# Outline of a Method for Determining the Three Dimensional Failure Route of a Sliding Block

Galic, D.

*galic@ce.berkeley.edu, University of California, Berkeley, USA*

Glaser, S.D.

*glaser@ce.berkeley.edu, University of California, Berkeley, USA*

Copyright 2005, ARMA, American Rock Mechanics Association

This paper was prepared for presentation at Alaska Rocks 2005, The 40th U.S. Symposium on Rock Mechanics (USRMS): Rock Mechanics for Energy, Mineral and Infrastructure Development in the Northern Regions, held in Anchorage, Alaska, June 25-29, 2005.

This paper was selected for presentation by a USRMS Program Committee following review of information contained in an abstract submitted earlier by the author(s). Contents of the paper, as presented, have not been reviewed by ARMA/USRMS and are subject to correction by the author(s). The material, as presented, does not necessarily reflect any position of USRMS, ARMA, their officers, or members. Electronic reproduction, distribution, or storage of any part of this paper for commercial purposes without the written consent of ARMA is prohibited. Permission to reproduce in print is restricted to an abstract of not more than 300 words; illustrations may not be copied. The abstract must contain conspicuous acknowledgement of where and by whom the paper was presented.

**ABSTRACT:** Starting with Patton and up through such recent workers as Grasselli and Egger, shear sliding models have been primarily concerned with the strength envelope developed along some predetermined linear path. While easily reproduced in a laboratory environment, this type of failure is a specialized case of general sliding. Large structures composed of individual blocks, most notably dams, are sometimes not restricted to one dimensional failure routes. As evidenced by Malpasset and other events, certain foundation conditions may result in blocks undergoing motion along non-linear paths. In this paper, we develop a geometric method for tracking a reference point on a sliding body. Specifically, we consider the case of three point contact resulting from the shear failure of a matching 3-plane foundation interface. Given a known hydrostatic driving force, and the constant moment resulting from center of mass eccentricity, we propose an incremental method for determining the spatial path of a monolith sliding upon a simple discretized surface. We also discuss the idea of superimposing different strength criteria along the calculated path, and emphasize the importance of the solution to energy infrastructure design and maintenance.

## 1. INTRODUCTION

The sliding stability of a gravity dam is derived from friction between dam monoliths and the underlying rock. Design frictional strength is in turn largely due to the local topography of the rock-concrete interface. It was Patton [1] who first introduced the effects of topography into Coulomb's law, through roughness coefficient  $i$ . Further modifications to the classic friction relation were made by Ladanyi and Archambault [2], Rengers and Fecker [3], and Barton [4]. These and other workers studied the effects of dilatancy, scaling, and quantified roughness within the two-dimensional framework of Coulomb's law. Recently, there have been several efforts to introduce objective surface parameters into a sliding model through the use of optical scanners. Among the most elegant is Grasselli and Egger 2002 [5] which proposes a simple, Patton-like equation involving both measured and statistical parameters.

The authors of [5] attempt to generalize their model by shearing "along different directions". This involves varying the angle between linear shear paths and using surface data specific to each line. The authors present this directional surface data on a polar diagram, which they feel "could become a useful qualitative tool. . . for the easy determination of directional behavior." But each of the hypothetical shear paths is a straight line! Thus in reality [5] like its predecessors remains grounded in two dimensional stress-displacement space.

Many of the above-mentioned models were developed to predict or substantiate results obtained from a direct shear device. In a laterally constrained direct shear test, the sample is free to move within a single vertical plane; forward motion and dilation are confined to this plane. Such boundary conditions simulate, for example, the failure route of some critical dam monolith sliding between two stable neighboring monoliths. This kind of buttressing stability cannot always be guaranteed.

On the brink of an incipient failure involving multiple blocks, lateral contact forces are progressively diminished and each block has the potential to slide in a semi-constrained or fully unconstrained manner. This type of scenario was realized in the 1959 Malpaset disaster, where the failure of an abutment assumed to be rigid led to the collapse of the dam.

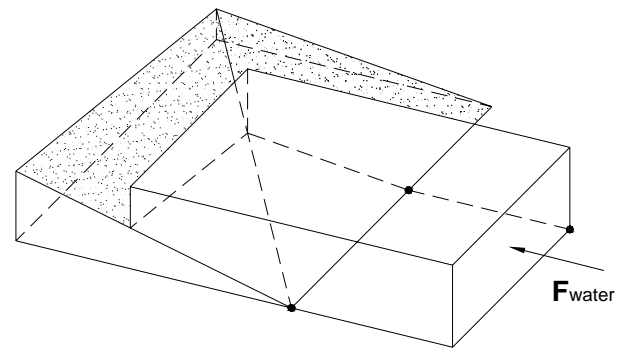
On the one hand, it makes little apparent sense to study the failure route of a dam monolith. In an environment where sliding on the order of inches may constitute failure, greater displacements become impossible to mitigate and wholly uninteresting to the health of the now worthless structure. On the other hand, knowledge of a preferred failure route may lend itself to specific types of preventive reinforcement, especially in an existing dam. And in the construction of a new dam, where the selection of monolith widths and locations is more or less flexible, an optimal configuration might exist, one which best takes advantage of foundation topography to reduce the likelihood of failure. For example, if a pair of adjacent monoliths having width  $w$  exhibit a tendency to slide freely in opposite directions, increasing their width to  $1.5w$  might capture enough variable topography to actually render them mutually self-supporting. In order to anticipate any of this, we need to develop a sliding model which predicts three-dimensional failure route.

In this paper, we consider an idealized dam foundation consisting of a horizontal surface and two oblique planes. Embracing the assumption of three-point contact, we examine what happens to a matching cast monolith as it is pushed along the foundation by hydraulic pressure acting on its upstream face. The driving hydraulic force vector operates through a vertical plane midway between the sides of the monolith. The monolith as a whole is volumetrically asymmetric, and its center of mass (CM) does not lie on the vertical median plane. This skewness results in a moment about the CM, and causes the monolith to stray from a linear trajectory. Motion thus occurs in all three cartesian directions. By relating the tilt of the monolith to linear and angular displacement in the horizontal plane, we develop a method for tracking a reference point (the center of mass) over the course of the sliding event. A moving, local coordinate system is established to facilitate computation of contact reactions. Computation of the spatial failure route is recursive and incremental.

## 2. PROBLEM SETUP

Consider a simple dam foundation with three distinct inclination planes. A monolith has been cast onto the foundation so that the two have a matching interface. Figure 1 (top) shows a schematic of this configuration, as well as the direction along which the hydraulic force is acting. In the event of failure at the monolith-foundation interface, the monolith will slide forward and up along the surface of the foundation. At the instant when motion is initiated, contact forces cease to act across the static contact surface and become confined to three discrete contact areas, marked as black dots in the figure. This topological fact can be ascertained by constructing a paperboard model; whether a given insitu monolith would fracture under three point bending is beyond the scope of this discussion, whose aim is to outline a geometrical approach to foundation stability. Rigid body motion is assumed.

Monolith



Model as . . .

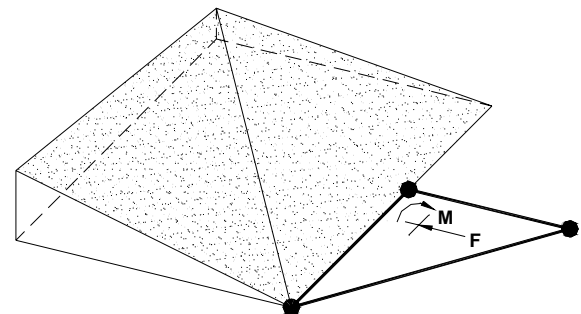


Figure 1. Monolith and foundation. Black dots indicate incipient contact points.

Because the entire succeeding interaction between monolith and foundation is limited to three discrete contact points, it seems inefficient to analyze the monolith as a whole. Rather, we model the monolith with a triangular frame, whose vertices represent contact points and whose perimeter contains the monolith's projected center of mass (Figure 1, bottom). The actual center of mass lies somewhere above the frame, as the dam has finite height. For the demonstrative purposes of this paper, we place both the center of mass and the driving force vector in the plane of the frame. This simplification is not unreasonable for a shallow monolith, and preserves the inplane moment about CM.

Figure 2 shows an aerial view of the frame and adjacent portions of the foundation. Prior to the start of sliding, the origins of both global and local coordinate systems are located at the center of mass. As the frame slides forward, the local coordinate system stays attached to CM,  $x'$  and  $z'$  axes remaining within the plane of the frame and parallel to the frame's shorter sides. Also shown in Figure 2 are the lines of intersection between foundation planes. The intersection line between planes 1 and 2 is shown in projection, and is not used for purposes of triangulation. Only the true horizontal lines of intersection are used for triangulation, as they represent the strike of planes 1 and 2.

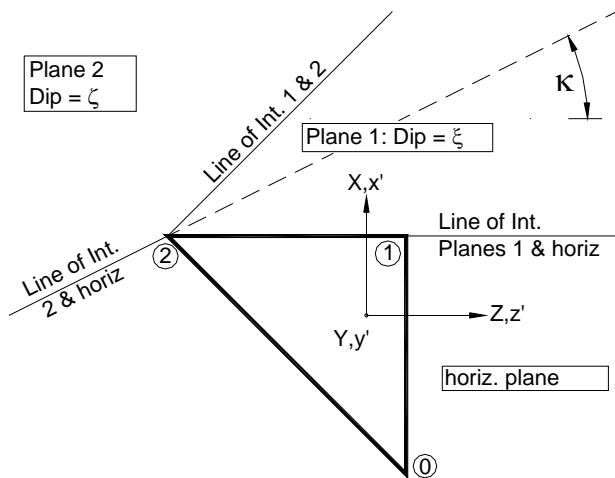


Figure 2. Aerial view of the frame and foundation.

At the moment when motion is incipient, each of the contact points appears to lie in the horizontal plane. However, as seen in Figure 2, even the slightest displacement will cause contact points 1 and 2 to move onto planes 1 and 2, respectively. We are interested only in those failure

routes wherein *contact points remain on their respective planes throughout the sliding event*. This restriction allows for a wide range of physical motion. The scenario of contact point 0 reaching one of the inclined planes involves such a large displacement that it precludes further analysis; the failure route beyond here is more or less irrelevant to the objective of preventive reinforcement or construction. Contact point 2 is much closer to plane 1 at any given moment. However, as the general trend of motion is forward (along the global  $X$  direction), it is reasonable to assume that increasing displacement maintains a separation between this contact point and the adjacent line of intersection.

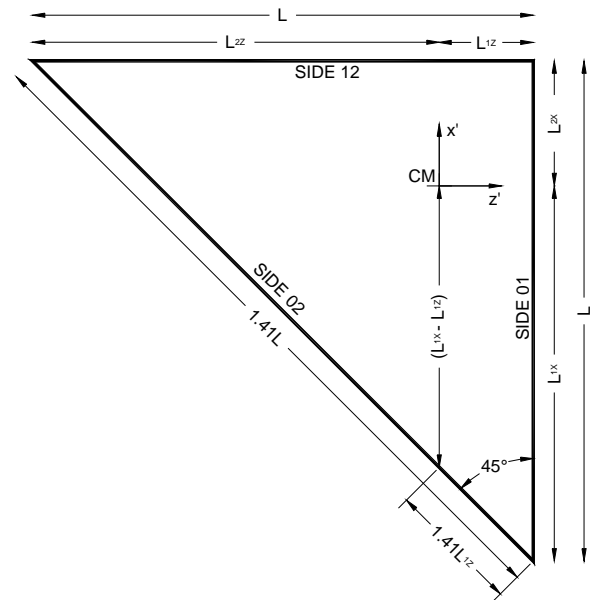


Figure 3. Frame dimensions.

We are considering rigid body motion. As displacement occurs, the dimensions of the frame (Figure 3) remain the same within the moving plane of the frame. Viewed from above however, in horizontal projection, the frame is no longer a right triangle. Angles have changed and the sides become foreshortened. Figure 4 shows the instant of sliding when the center of mass has been displaced by  $X$  and  $Z$  units. Furthermore, the projection of side 01 (as well as the projection of the  $x'$  axis) has been rotated through an angular displacement  $\theta$ . In one sense this rotation follows from contact interaction with the topography, but it is primarily the result of monolith eccentricity. As the monolith slides, pitches, and rotates, hydraulic pressure continues to act on the upstream face so long as there is water

behind the dam. Net hydraulic force  $\mathbf{F}$  operates along the center line of the monolith, parallel to local axis  $x'$ . Owing to monolith asymmetry,  $\mathbf{F}$  does not pass directly through the center of mass. The offset is a constant distance  $c$ , resulting in a constant moment  $\mathbf{M}$  about the  $y'$  axis ( $M = cF$ ).

As the frame undergoes displacement, each of its sides becomes inclined with respect to the horizontal plane. For a given displacement ( $X, Z, \theta$ ),

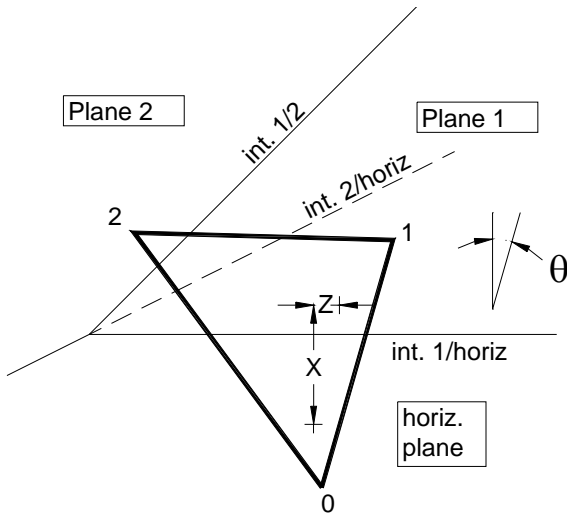


Figure 4. Displaced frame.

the vertical angles beneath sides 01, 02, and 12 are  $\alpha(X, Z, \theta)$ ,  $\beta(X, Z, \theta)$ , and  $\gamma(X, Z, \theta)$  respectively. Solving for these angles allows us to calculate the elevation of CM, giving a complete position vector in terms of the displacements. Figure 5 shows the displaced configuration of the triangle as viewed in

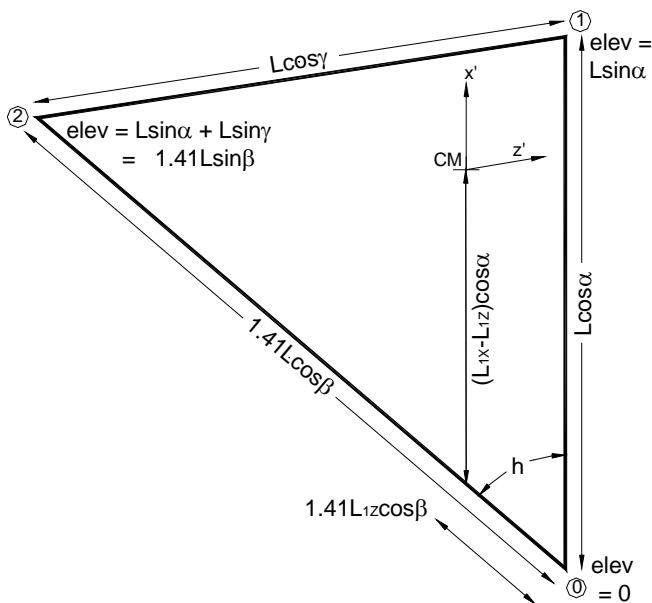


Figure 5. Displaced configuration.

projection. The sides of the triangle, whose inplane lengths are  $L, L$  and  $1.41L$ , appear to have lengths  $L \cos \alpha, L \cos \gamma$ , and  $1.41L \cos \beta$ . A relationship between  $\alpha, \beta$ , and  $\gamma$  follows from the frame geometry. Contact point 2 can be reached from point 0 by moving directly along side 02 or along sides 01 and 12. The net elevation gain must be the same, and so  $L \sin \alpha + L \sin \gamma = 1.41L \sin \beta$ , or,

$$\gamma = \arcsin(1.41 \sin \beta - \sin \alpha). \quad (1)$$

The interior projection angle between sides 01 and 02, denoted as  $h$ , can be computed using the law of cosines and (1) as

$$\cos(h) = \frac{\cos 45 - \sin \alpha \sin \beta}{\cos \alpha \cos \beta}. \quad (2)$$

Angle  $h$  is a known function of unknown angles  $\alpha$  and  $\beta$ .

### 3. TRIANGULATING THE PROJECTION FRAME

Our objective is to calculate  $\alpha$  and  $\beta$  in terms of the applied displacements. One way to do this is by applying the law of sines to vertical edge profiles (Figure 6), each of which describe a triangle consisting of frame edge, horizontal plane, and inclined plane.  $\xi'$  and  $\zeta'$  are the apparent dips of planes 1 and 2 beneath sides 01 and 02. They depend on  $\theta$  and, in the case of  $\zeta'$ , on the instantaneous value of  $h$ . Note that in the profile of

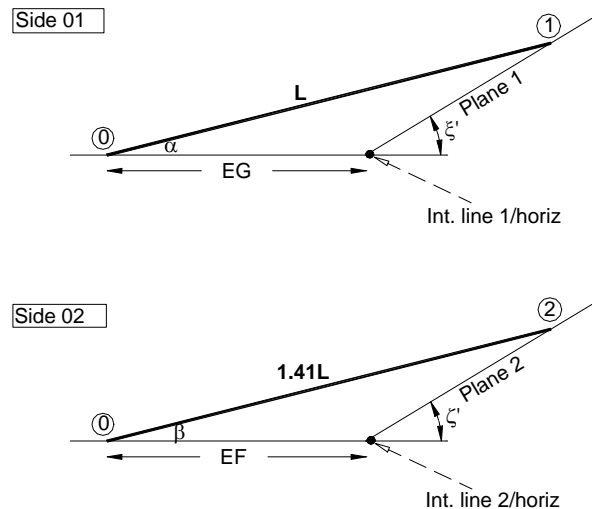


Figure 6. Edge profiles.

side 02, plane 1 does not appear, even though side 02 crosses over plane 1 before reaching contact point 2 (see Fig. 4). In fact, we are disregarding both plane 1 and intersection line 1/2 (a prominent topographic feature). This is possible because we have restricted contact point 2 motion to the visible portion of plane 2. Distances along side 02 are referenced to the hidden intersection line 2/horiz; from the perspective of contact 2, plane 1 does not exist.

The triangles in Figure 6 have one known length (frame edge) and one known angle (apparent dip). To determine the length of horizontal sides, we must refer to the projection frame, as shown in Figure 7. The distances of interest here are EF and EG. These must be related to  $X$ ,  $Z$ ,  $\theta$ , and known functions of  $\alpha$  and  $\beta$ . It is a fairly simple matter to relate EG to displacement  $X$  and the projected frame dimensions. The distances  $DO'$  and  $DE$  are taken directly from Figure 5. The distance from  $O$  to int. line 1/horiz is fixed at  $L_{2X}$  (recall that the global origin was originally coextensive with CM). Projecting  $DO'$ ,  $DE$  onto the global  $X$  axis, subtracting displacement  $X$  and adding  $L_{2X}$ , we have

$$EG \cos \theta = 1.41L_{1Z} \cos \beta \cos(h - \theta) + (L_{1X} - L_{1Z}) \cos \alpha \cos \theta + L_{2X} - X. \quad (3)$$

The relationship between the displacements and length EF is not so immediately apparent. Because the location of point F is itself unknown, we cannot

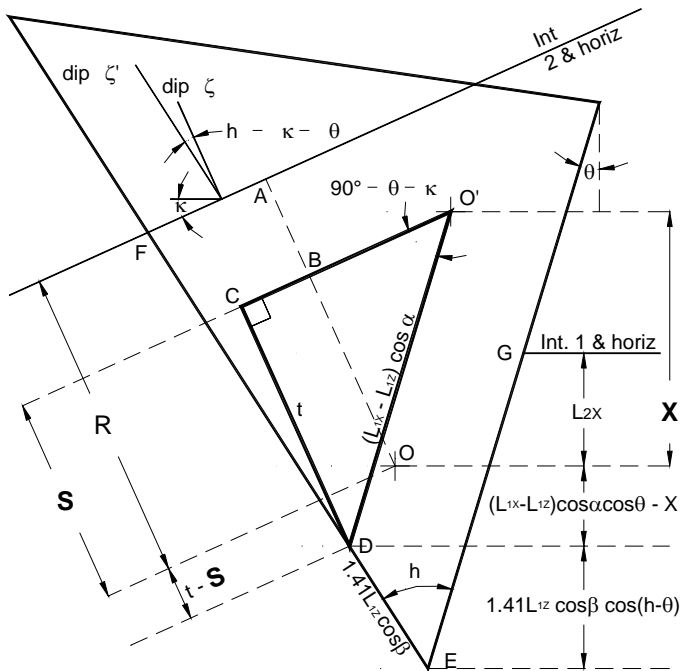


Figure 7. Triangulation of the projection frame.

simply project existing dimensions onto side 02. It becomes necessary to define two additional parameters.

As mentioned above, the distance from  $O$  to int. line 1/horiz is fixed at  $L_{2X}$ . This follows directly from the dimensions of the frame, because side 12 is initially flush with int. line 1/horiz, and  $O'$  (the CM) coextensive with  $O$ . The minimum distance from  $O$  to int. line 2/horiz is likewise fixed. Drawing a line through  $O$  and parallel to the plane 2 dip direction (Figure 8), we can compute this distance as

$$R = L_{2X} \cos \kappa + L_{2Z} \sin \kappa, \quad (4)$$

where  $\kappa$  is the azimuth of int. line 2/horiz. Taking  $\text{dipdir}_2$  ( $\perp$  int. line 2/horiz) as our new displacement direction,  $X$  and  $Z$  can be parametrized into a single variable  $S$  (Fig. 9):

$$S = X \cos \kappa - Z \sin \kappa. \quad (5)$$

$S$  is the distance from  $O$  to a line running through  $O'$  and parallel to  $\text{strike}_2$  ( $=$  int. line 2/horiz).

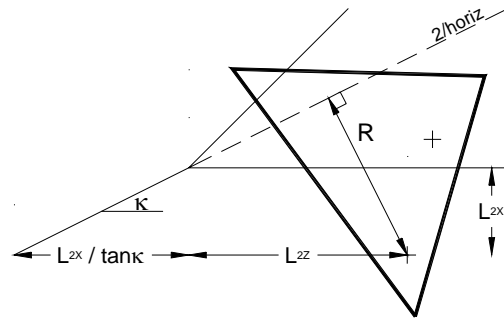


Figure 8. Parameter R.

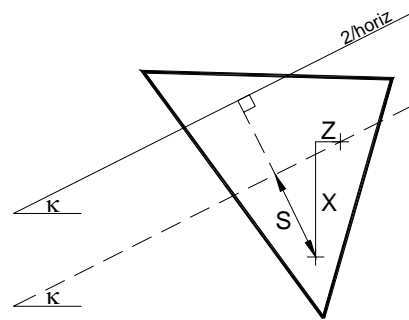


Figure 9. Parameter S.

We are now ready to compute distance EF (Figure 7). Let  $C$  be the point of intersection of a line running through  $D$ , parallel to  $\text{dipdir}_2$ , and a

line running through O', parallel to strike<sub>2</sub>. Distance CD is given by

$$t = (L_{1X} - L_{1Z}) \cos \alpha \sin(90^\circ - \theta - \kappa). \quad (6)$$

It follows from Figure 7 that

$$DF \cos(h - \kappa - \theta) = R + t - S, \quad (7)$$

and so we have

$$EF = 1.41L_{1Z} \cos \beta + (R + t - S) \sec(h - \kappa - \theta). \quad (8)$$

It is now possible to apply the law of sines.

#### 4. COUPLED SOLUTION PAIR

The triangles shown in Figure 6 now have two known sides and one known angle, the apparent dip. By applying the law of sines, we can relate  $\alpha$ ,  $\beta$  to their own functions and to global displacements. Noting that  $\sin(180^\circ - \xi) = \sin(\xi)$ , we have

$$\frac{\sin \xi'}{L} = \frac{\sin(\xi' - \alpha)}{EG}, \quad (9)$$

$$\frac{\sin \zeta'}{1.41L} = \frac{\sin(\zeta' - \beta)}{EF}. \quad (10)$$

The apparent dip  $\xi'$  depends only on  $\theta$  and is given (see for example [6]) by

$$\tan \xi' = \tan \xi \cos \theta. \quad (11)$$

The apparent dip  $\zeta'$  is a function of projection angle  $h$ , and hence of  $\alpha$  and  $\beta$ :

$$\tan \zeta' = \tan \zeta \cos(h - \kappa - \theta). \quad (12)$$

Using (3), (8), (11) and (12), Equations (9) and (10) can be written as

$$\begin{aligned} 1.41L_{1Z} \cos \beta \cos(h - \theta) = \\ X - L_{2X} - (L_{1X} - L_{1Z}) \cos \alpha \cos \theta \\ + L \cos \theta \cos \alpha - L \cot \xi \sin \alpha, \end{aligned} \quad (13)$$

$$\begin{aligned} 1.41L_{2Z} \cos \beta \cos(h - [\kappa + \theta]) = \\ 1.41L \sin \beta \cot \zeta + R + t - S. \end{aligned} \quad (14)$$

Recall that

$$\cos(h) = \frac{\cos 45 - \sin \alpha \sin \beta}{\cos \alpha \cos \beta}.$$

Transcendental functions of  $h$  must be expanded and expressed in terms of  $\alpha$  and  $\beta$ .

As stated, our simple discretized dam foundation consists of a horizontal plane and two oblique planes. The maximum values attainable by  $\alpha$  and  $\beta$  are  $\xi$  and  $\zeta$ , the true dip angles of planes 1 and 2. These represent limiting values achieved only when contact points reach the end of their allowable sliding domains. For most of the sliding event, the values of  $\alpha$  and  $\beta$  are substantially less than  $\xi$  and  $\zeta$ . If foundation inclination values themselves are relatively small (0-30°), then it makes sense to use the small angle approximations, as these greatly simplify our problem. Thus we approximate  $\sin \alpha$ ,  $\sin \beta$  as  $\alpha$ ,  $\beta$ , and  $\cos \alpha$ ,  $\cos \beta$  as 1. Following this simplification and rearrangement, equations (13) and (14) take the form

$$f_1 + f_2 \alpha + f_3 \alpha \beta + f_4 \alpha^2 + f_5 \alpha^2 \beta + f_6 \alpha^2 \beta^2 = 0,$$

$$f_7 + f_8 \beta + f_9 \alpha \beta + f_{10} \beta^2 + f_{11} \alpha \beta^2 + f_{12} \alpha^2 \beta^2 = 0, \quad (15a, 15b)$$

where

$$f_1 = X^2 + 2L_{2X}(\cos \theta - 1)X + (L_{2X}^2 - L_{1Z}^2) \sin^2 \theta,$$

$$f_2 = 2L \cot \xi (L_{2X} - X - \cos \theta [L_{2X} + L_{1Z}]),$$

$$f_3 = 2\sqrt{2}L_{1Z}(\cos^2 \theta [L_{1Z} + L_{2X}] - \cos \theta [L_{2X} - X] - L_{1Z}),$$

$$f_4 = L^2 \cot^2 \xi,$$

$$f_5 = -2\sqrt{2}LL_{1Z} \cos \theta \cot \xi,$$

$$f_6 = 2L_{1Z}^2,$$

$$f_7 = D^2 - 2L_{2X} \cos(\theta + \kappa)D$$

$$+ \cos^2(\theta + \kappa)(-L_{2X} + 2L_{2Z})^2 - L_{2Z}^2 \sin^2(\theta + \kappa),$$

$$f_8 = 2\sqrt{2}L \cot \zeta (D - L_{2X} \cos[\theta + \kappa]),$$

$$f_9 = 2\sqrt{2}L_{2Z}(\cos^2[\theta + \kappa][L_{1X} - L_{1Z}] + D \cos[\theta + \kappa] - L_{2Z}),$$

$$f_{10} = 2L^2 \cot^2 \zeta,$$

$$f_{11} = 4LL_{1Z} \cos(\theta + \kappa) \cot \zeta,$$

$$f_{12} = 2L_{2Z}^2,$$

and  $D = R - S = \cos \kappa (L_{2X} - X) + \sin \kappa (L_{2Z} + Z)$ .

Equations (15a) and (15b) both contain fourth degree polynomials. They represent a coupled system with up to 16 solution pairs  $(\alpha, \beta)$  per increment. Some of these are repeated and others complex-valued. We are interested only in positive real-valued solution pairs which lie in the range  $(0, \xi; 0, \zeta)$ . This filters out a large number of extraneous solutions, but how does one choose between multiple valid solutions? There is certainly the intuitive approach of gradually expanding the range of interest as sliding progresses. For example, during an early increment, solutions closer to  $(0, 0)$  would be more reasonable than solutions close to  $(\xi, \zeta)$ . Problems arise when this type of selection must be automated, repeated once in every increment and consistent with the results of neighboring increments. For the purposes of this paper, we will ignore the numerically important question of solution uniqueness and assume that system (15) yields exactly one valid solution pair per increment.

## 5. ESTABLISHING A LOCAL COORDINATE SYSTEM

In the preceding, calculations have been made in terms of the global displacements  $X$  and  $Z$ . Once inclination angles  $\alpha$  and  $\beta$  have been computed within an increment, it becomes possible to define a local coordinate system that remains attached to the center of mass throughout sliding. This becomes particularly convenient for calculating tip reactions, as resultant moments and forces all act through CM.

Placing the origin of our local coordinate system at the center of mass, we define the  $x'$  axis as a ray in the direction of side 12, parallel to side 01 (Figure 3). The  $z'$  axis is in the direction of side 01, parallel to side 12. Axis  $y'$  is normal to the frame as given by right hand convention. We can write the local unit vectors  $\mathbf{i}'$  and  $\mathbf{k}'$  in terms of global unit vectors  $\mathbf{i}, \mathbf{j}, \mathbf{k}$ , calculated angles  $\alpha, \gamma$ , and angular displacement  $\theta$ :

$$\mathbf{i}' = \cos \alpha \cos \theta \mathbf{i} + \sin \alpha \mathbf{j} + \cos \alpha \sin \theta \mathbf{k}, \quad (16)$$

$$\mathbf{k}' = \cos \gamma \sin \theta \mathbf{i} + \sin \gamma \mathbf{j} + \cos \gamma \cos \theta \mathbf{k}. \quad (17)$$

Local unit vector  $\mathbf{j}'$  is given by the cross product  $\mathbf{k}' \times \mathbf{i}'$  as

$$\begin{aligned} \mathbf{j}' = & (\cos \alpha \sin \gamma \sin \theta - \sin \alpha \cos \gamma \cos \theta) \mathbf{i} \\ & + (\cos \alpha \cos \gamma \cos^2 \theta - \cos \alpha \cos \gamma \sin^2 \theta) \mathbf{j} \\ & + (\sin \alpha \cos \gamma \sin \theta - \cos \alpha \sin \gamma \cos \theta) \mathbf{k}. \end{aligned} \quad (18)$$

In general, the transformation between local  $(x', y', z')$  and global  $(X, Y, Z)$  coordinate systems is given by

$$\mathbf{v}_{local} = \mathbf{R} \mathbf{v}_{global}, \quad (19)$$

where  $\mathbf{R}$  is the global transformation matrix defined as  $R_{ij} = \mathbf{e}'_i \cdot \mathbf{e}_j$  or,

$$\mathbf{R} = \begin{bmatrix} \cos \alpha \cos \theta & \sin \alpha & \cos \alpha \sin \alpha \\ \left( \begin{array}{c} \cos \alpha \sin \gamma \\ * \sin \theta - \\ \sin \alpha \cos \gamma \\ * \cos \theta \end{array} \right) & \left( \begin{array}{c} \cos \alpha \cos \gamma \\ * \cos^2 \theta - \\ \cos \alpha \cos \gamma \\ * \sin^2 \theta \end{array} \right) & \left( \begin{array}{c} \sin \alpha \cos \gamma \\ * \sin \theta - \\ \cos \alpha \sin \gamma \\ * \cos \theta \end{array} \right) \\ \cos \gamma \sin \theta & \sin \gamma & \cos \gamma \cos \theta \end{bmatrix}$$

By definition,  $\mathbf{R} = \mathbf{R}^{-1} = \mathbf{R}^T$  (see for example [7]). It follows that the inverse transformation is given by

$$\mathbf{v}_{global} = \mathbf{R}^T \mathbf{v}_{local}.$$

Having established a local coordinate system at the center of mass, we can refer to points on the frame in terms of the frame's own dimensions. Figure 10 shows the tip position vectors  $\mathbf{r}_0, \mathbf{r}_1$ , and  $\mathbf{r}_2$ . They are defined by

$$\begin{aligned} \mathbf{r}_0 &= -L_{1X} \mathbf{i}' + L_{1Z} \mathbf{k}', \\ \mathbf{r}_1 &= L_{2X} \mathbf{i}' + L_{1Z} \mathbf{k}', \\ \mathbf{r}_2 &= L_{2X} \mathbf{i}' - L_{2Z} \mathbf{k}'. \end{aligned} \quad (20)$$

Also shown in Figure 10 is the global position vector  $\mathbf{r}_{cm}$ , which locates the center of mass in terms of global displacements. It is written as

$$\mathbf{r}_{cm} = X \mathbf{i} + (1.41 L_{1Z} \sin \beta + [L_{1X} - L_{1Z}] \sin \alpha) \mathbf{j} + Z \mathbf{k}. \quad (21)$$

By recording the value of  $\mathbf{r}_{cm}$  in every temporal increment, we obtain a three-dimensional time dependent path for the center of mass during sliding.

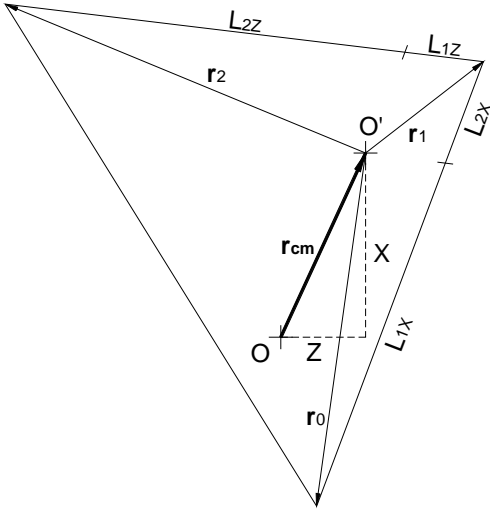


Figure 10. Internal position vectors.

## 6. CALCULATING REACTIONS

Once sliding begins, all interaction between monolith and dam foundation is confined to three discrete contact points. The hydraulic force  $\mathbf{F}$ , induced moment  $\mathbf{M}$  and weight of the monolith  $\mathbf{W}$  are resisted by normal ( $\mathbf{N}$ ) and shear ( $\mathbf{S}$ ) reactions at the tips (Figure 11). Written in local coordinates, these are

$$\begin{aligned} \mathbf{S}_0 &= a\mathbf{i}' + b\mathbf{j}' + c\mathbf{k}', \\ \mathbf{S}_1 &= d\mathbf{i}' + e\mathbf{j}' + f\mathbf{k}', \\ \mathbf{S}_2 &= g\mathbf{i}' + h\mathbf{j}' + i\mathbf{k}', \end{aligned} \quad (22a)$$

$$\mathbf{N}_0 = j\hat{\mathbf{n}}_0, \quad \mathbf{N}_1 = k\hat{\mathbf{n}}_1, \quad \mathbf{N}_2 = l\hat{\mathbf{n}}_2, \quad (22b)$$

where  $a$  through  $l$  are twelve unknown constants and  $\hat{\mathbf{n}}$  are the unit normals. Acceleration within a given increment is restricted to the local  $x'$  direction, and rotation confined to the  $y'$  axis. We thus have

$$\left. \begin{aligned} \sum \mathbf{M} &= I_m A \mathbf{j}' \\ \sum \mathbf{F} &= m a \mathbf{i}' \end{aligned} \right\} \quad (\text{four free equations}) \quad (23)$$

where the contribution of contact point  $i$  to net moment is given by  $\mathbf{r}_i \times (\mathbf{S}_i + \mathbf{N}_i)$ .  $I_m$  is the mass moment of inertia of the monolith (frame only in this case) and  $A$  the still uncalculated magnitude of angular acceleration about  $y'$ . Six additional equations arise from fundamental relationships between  $\mathbf{S}$  and  $\mathbf{N}$ . These are:

$$\left. \begin{aligned} \mathbf{S}_{0,1,2} \cdot \mathbf{N}_{0,1,2} &= 0, \\ |\mathbf{S}_{0,1,2}| &= \mu_k |\mathbf{N}_{0,1,2}|, \end{aligned} \right\} \quad (\text{six equations}) \quad (24a,b)$$

where  $\mu_k$  is the interface coefficient of dynamic friction as applied to Mohr-Coulomb sliding (a discussion of this follows). Having thus ten equations for twelve unknowns, we are two equations short. In order to solve for the reactions, we need to make some assumptions that will reduce the number of unknown constants by two. One not unreasonable assumption is that proportions between  $\mathbf{N}_0$ ,  $\mathbf{N}_1$ ,  $\mathbf{N}_2$ , achieved during *frictionless* sliding (sliding without shear reactions) remain the same during frictional sliding. In a given increment, the reactions during *frictionless* sliding are

$$\mathbf{N}_0^S = c_0 \hat{\mathbf{n}}_0, \quad \mathbf{N}_1^S = c_1 \hat{\mathbf{n}}_1, \quad \mathbf{N}_2^S = c_2 \hat{\mathbf{n}}_2, \quad (25)$$

subject to

$$\sum \mathbf{F} \cdot \mathbf{j}' = 0, \quad \sum \mathbf{M} \cdot \mathbf{i}' = 0, \quad \sum \mathbf{M} \cdot \mathbf{k}' = 0, \quad (26)$$

a simple statically determinate system. Having solved for  $\mathbf{N}_0^S$ ,  $\mathbf{N}_1^S$ ,  $\mathbf{N}_2^S$ , the ratios of interest are

$$m_1 = \frac{|\mathbf{N}_1^S|}{|\mathbf{N}_0^S|}, \quad m_2 = \frac{|\mathbf{N}_2^S|}{|\mathbf{N}_0^S|}. \quad (27)$$

Assuming these proportions remain constant during frictional sliding, expression (22b) becomes

$$\mathbf{N}_0 = j\hat{\mathbf{n}}_0, \quad \mathbf{N}_1 = jm_1\hat{\mathbf{n}}_1, \quad \mathbf{N}_2 = jm_2\hat{\mathbf{n}}_2. \quad (28)$$

The number of unknown constants in (22) has now been reduced to ten. Using (23) and (24), normal and shear reactions are calculated. Once the reactions are known, (23) is again used to find the linear and angular accelerations.

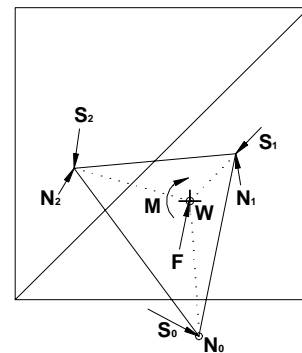


Figure 11. Tip reactions.

## 7. INCREMENTAL SOLUTION

It should be noted that the problem under consideration is more than just a stability analysis with unusually tricky geometry. We are dealing with an object (monolith) that has multiple contact points on multiple surfaces yet, at any given instant, can only travel in a single collective direction. As a result, the net velocity of the monolith,  $\mathbf{v}_{cm}$ , inevitably points into one of the oblique surfaces ie.,

$$\mathbf{v}_{cm} \cdot \hat{\mathbf{n}}_{1,2} \neq 0. \quad (29)$$

Equation (29) is characteristic of an *impact* problem. Impact (see for example [8]) is a complex phenomenon involving material properties, time effects, and numerically difficult computation. Even a relatively simple case like the Painlevé example (toppling rod) leads to bifurcation, indeterminacy, and a host of other issues which can hopelessly clutter an already difficult analysis.

We avoid these issues by adapting an incremental approach. Whereas the cumulative trajectory of the monolith must constantly be changing from surface interaction, incremental displacements along the local x' axis are inherently one-dimensional. This means that incremental motion temporarily results in “buried” contact points. Their location is reinitialized at the start of each increment, because of the way in which we calculate CM position. Absolute displacements  $X$ ,  $Z$  and  $\theta$  are completely independent of whatever may be happening on the surface, and true dip values  $\xi$  and  $\zeta$  remain the same throughout sliding. These parameters are used to compute inclination angles and ultimately the vertical coordinate of CM. Once global incremental displacements  $dX$ ,  $dZ$ , and  $d\theta$  are absorbed into the updated absolute position, the problem is reduced to a geometric construction.

We thus employ an incremental approach to calculating the CM position. The choice of temporal rather than spatial increments has been made less for the sake of a time dependent path (see discussion) than for practical reasons.  $dX$ ,  $dZ$  and  $d\theta$  can be easily expressed as functions of time, whereas the task of making  $t$  and  $\theta$  functions of  $dX$  and  $dZ$  is unwieldy. We now have all the requisite components necessary for an iterative computation of the sliding monolith’s failure route. The method is outlined as follows.

Increment  $q$ :  $t \in (t_{q-1}, t_q)$ ;  $q \in (1, 2, 3, \dots)$

- The truss CM is located at  $\mathbf{r}_{cm}(q-1)$
- Local coordinate system defined by  $\mathbf{i}'(q-1)$ ,  $\mathbf{j}'(q-1)$ ,  $\mathbf{k}'(q-1)$
- The transformation matrix is  $\mathbf{R}(q-1)$
- The driving force is  $\mathbf{F}_{hydro}(q-1)$ , driving moment  $\mathbf{M}_{hydro}(q-1)$
- Calculate tip reactions
- Calculate net force along  $\mathbf{i}'(q-1) \rightarrow \mathbf{F}_{local}^q$
- Calculate net moment in  $\mathbf{j}'(q-1) \rightarrow \mathbf{M}_{local}^q$
- Transform  $\mathbf{F}_{local}^q$ ,  $\mathbf{M}_{local}^q$  into global coordinates:

$$\mathbf{F}_{global}^q = \mathbf{R}^T(q-1)\mathbf{F}_{local}^q,$$

$$\mathbf{M}_{global}^q = \mathbf{R}^T(q-1)\mathbf{M}_{local}^q.$$

- $F_X^q = \mathbf{F}_{global}^q \cdot \mathbf{i}$  (30)

- $F_Z^q = \mathbf{F}_{global}^q \cdot \mathbf{k}$  (31)

- $M_Y^q = \mathbf{M}_{global}^q \cdot \mathbf{j}$  (32)

- $a_X^q = F_X^q / m$ ,  $v_X^q = v_X^{q-1} + a_X^q t$  (33a,b)

- $a_Z^q = F_Z^q / m$ ,  $v_Z^q = v_Z^{q-1} + a_Z^q t$  (34a,b)

- $A_X^q = M_Y^q / I_m$ ,  $\omega_Y^q = \omega_Y^{q-1} + A_Y^q t$  (35a,b)

- $X_{cm}^q = X_{cm}^{q-1} + v_X^{q-1} t + 0.5 a_X^q t^2$  (36)

- $Z_{cm}^q = Z_{cm}^{q-1} + v_Z^{q-1} t + 0.5 a_Z^q t^2$  (37)

- $\theta_{cm}^q = \theta_{cm}^{q-1} + \omega_Y^{q-1} t + 0.5 A_Y^q t^2$  (38)

- calculate  $\alpha(q)$ ,  $\beta(q)$ ,  $\gamma(q)$  by solving system (15)

- $\mathbf{r}_{cm}^q = X_{cm}^q \mathbf{i} + Z_{cm}^q \mathbf{k}$   
 $+ (1.41 L_{1Z} \sin \beta + [L_{1X} - L_{1Z}] \sin \alpha) \mathbf{j}$

- recalibrate local coordinate system:

$$\mathbf{i}'(q) = \cos \alpha^q \cos \theta^q \mathbf{i} + \sin \alpha^q \mathbf{j} + \cos \alpha^q \sin \theta^q \mathbf{k}$$

$$\mathbf{k}'(q) = \cos \gamma^q \cos \theta^q \mathbf{i} + \sin \gamma^q \mathbf{j} + \cos \gamma^q \sin \theta^q \mathbf{k}$$

$$\mathbf{j}'(q) = \mathbf{k}' \times \mathbf{i}'$$

- $R_{ij}(q) = \mathbf{e}_i'(q) \cdot \mathbf{e}_j(q)$  (39)

- $\mathbf{F}_{hydro}(q) = F_{hydro} \mathbf{i}'(q)$  (40)

- $\mathbf{M}_{hydro}(q) = M_{hydro} \mathbf{j}'(q)$  (41)

Figure 12 shows how a calculated path might look when viewed from above.

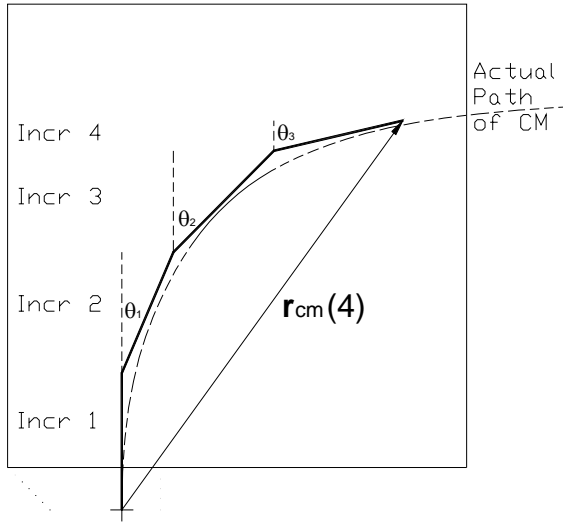


Figure 12. Sample calculated path.

## 8. DISCUSSION

In the preceding, we have outlined a method for determining the three-dimensional failure route of an asymmetric block sliding along a matching 3-plane interface. The quantitative description of failure route has been achieved sequentially: by calculating reactions over a number of temporal increments, by updating the instantaneous sliding direction, and by obtaining a global position vector for each increment. Taken collectively, the tips of these position vectors describe the path of the monolith CM.

Although each individual position vector is associated with a specific additive time value, the path we obtain is not necessarily a “time-dependant” one. In this formulation, time is used as a parameter rather than a variable; as applied in equations (33a)-(35a), it serves to give correct proportions between angular and linear accelerations. The subordinate calculation of incremental velocity (33b)-(35b) is necessary for achieving proportional displacements (36)-(38). Whether calculated velocity reflects the actual speed with which our monolith plummets is less important than the path taken thereby. Preventive and remedial construction measures depend more closely on the anticipated failure route than on the length of time over which failure occurs.

Friction, doubtless the most important factor in any stability analysis, was quietly introduced in equation (24b), as a fundamental relationship between normal and shear stresses. We have employed the basic “physics-textbook” relation for

dynamic friction,  $S = \mu_k N$ . Whereas static coefficient  $\mu_s$  is often regarded as the tangent of interface friction angle  $\phi_{joint}$ , a bilinear failure envelope must be considered in order to give  $\mu_k$  analogous meaning. When the asperities of a rough joint surface have been sheared through, displacement rate increases and the apparent friction angle drops from  $\phi_{joint}$  to  $\phi_{residual}$  (see [6] for a discussion of this). At the moment when our analysis begins, small scale asperities surrounding each contact point have already been sheared away and substantial displacement is occurring. Thus  $\mu_k$  in equation (24b) is essentially the tangent of  $\phi_{residual}$ .

In writing equation (24b), we have effectively adapted the Mohr-Coulomb view of sliding. As such, our model is a three-dimensional extension of Patton’s law, with dip angles  $\xi$  and  $\zeta$  replacing roughness coefficient  $i$ . The “roughness” here consists of the large scale topographic features of the dam foundation. In the present paper, we have ignored surface scale roughness as described by the  $JRC$  or average contact area. This has been done in the interest of brevity; there is nothing about our method that restricts it to one specific kind of friction criterion. Instead of writing

$$|\mathbf{S}_i| = \mu_k |\mathbf{N}_i|,$$

we might have used Barton and Choubey’s  $JRC$  equation [4],

$$\tau = \sigma \tan \left[ JRC \log_{10} \left( \frac{JCS}{\sigma} \right) + \phi_\mu \right], \quad (43)$$

normalized for each contact point as

$$|\mathbf{S}_i| = |\mathbf{N}_i| \tan \left[ JRC \log_{10} \left( \frac{JCS_{norm}}{|\mathbf{N}_i|} \right) + \phi_\mu \right],$$

thereby introducing surface-scale roughness information. In fact, equation (24b) can be replaced with any friction criterion involving proportional stresses (this is not the case for example with Ladanyi and Archambault’s equation in [2]). The possible importance of small scale roughness to our problem, the applicability of (43) to a single contact point, and the overall accuracy of our incremental procedure are issues that can only be addressed

thorough a physical testing program. A specialized, laterally unconstrained shear device is currently being developed for this purpose.

In closing, we would like to underscore the importance of the problem discussed here. Gravity dams (the most obvious application of our method) constitute a large percentage of water bearing structures. Many of the dams in service today were built at a time when accurate methods of dynamic analysis were time-involved and difficult. As structures age and are retrofitted, it becomes necessary to repeat the original calculations. This has been the case at Folsom Dam (east of Sacramento, California), where a recent effort to increase the reservoir capacity has led to a series of innovative shear tests [9]. One of the critical factors at Folsom is the manner in which the monoliths are arranged on irregular foundation topography. Discretized, the foundation surface lends itself to the type of analysis we have outlined. Future extensions of this work will be aimed at applying our basic 3-plane model to a general discretized surface with  $n$  planes, enabling us to analyze a wide range of existing dam foundations.

## 9. ACKNOWLEDGEMENTS

This research is funded by the National Science Foundation under grant CMS-0408389. The authors would like to thank professors Richard E. Goodman and Gen-Hua Shi for their assistance.

## REFERENCES

1. Patton, F.D. 1966. Multiple modes of shear failure in rock. In *Proc. 1<sup>st</sup> Cong. ISRM*, vol 1, Lisbon, p. 509.
2. Ladanyi, B., and G. Archambault. 1970. Simulation of shear behavior of a jointed rock mass. In *Proc. 11<sup>th</sup> Symposium on Rock Mechanics*, AIME, p.105.
3. Fecker, E., and N. Rengers. 1971. Measurement of large scale roughness of rock planes by means of profilograph and geological compass. In *Proc. Int. Symp. On Rock Fracture*, Nancy (ISRM), paper 1-18.
4. Barton, N.R., and V. Choubey. 1977. The shear strength of rock joints in theory and practice. *Rock Mechanics* 10: p. 1.
5. Grasselli, G., and P. Egger. 2002. Constitutive law for the shear strength of rock joints based on three-dimensional surface parameters. *International Journal of Rock Mechanics* 40: p. 25.
6. Goodman, R.E. 1989. *Introduction to Rock Mechanics*, 2<sup>nd</sup> ed. New York: Wiley.
7. Ginsberg, J.H. 1995. *Advanced Engineering Dynamics*, 2<sup>nd</sup> ed. Cambridge: Cambridge Univ. Press.
8. Brogliato, B. 1999. *Nonsmooth Mechanics*. London: Springer-Verlag.
9. Goodman, R.E., and A. Bro. 2005. Shear strength of a foundation with two dimensional roughness. In *Proc. 40<sup>th</sup> U.S Rock Mechanics Symposium*, ARMA, paper 799.